





Evolution of antiferromagnetism in Zn-doped heavy-fermion compound $\text{CeRh}(\text{In}_{1-x}\text{Zn}_x)_5$

Tae Beom Park,¹ Soohyeon Shin,¹ Sangyun Lee^{1,2},, Soonbeom Seo^{1,2},, Harim Jang,¹ Jihyun Kim¹,, Hyoyoung Lee^{1,3},
Honghong Wang,¹ Hanoh Lee,¹ and Tuson Park^{1,*}

¹Center for Quantum Materials and Superconductivity (CQMS) and Department of Physics, Sungkyunkwan University, Suwon 16419, South Korea

²Los Alamos National Laboratory - Los Alamos, New Mexico 87545, USA

³Centre for Integrated Nanostructure Physics (CINAP), Institute of Basic Science (IBS), Department of Chemistry, Sungkyunkwan University, Suwon 16419, South Korea



(Received 16 January 2020; revised 19 June 2020; accepted 14 July 2020; published 18 August 2020)

We report the dependence of antiferromagnetism on Zn-doping concentration in the newly synthesized $\text{CeRh}(\text{In}_{1-x}\text{Zn}_x)_5$ single crystal with $x \leq 0.023$. X-ray-diffraction measurements showed a smooth decrease of lattice parameters with an increasing Zn concentration, indicating a positive chemical pressure effect. The electrical resistivity, specific heat, and magnetic susceptibility measurements revealed that the antiferromagnetic transition temperature T_N initially decreases from 3.8 K for pure CeRhIn_5 to 3.1 K at $x = 0.012$; then, it becomes flat, remaining at approximately 3.1 K between Zn concentrations of 0.012 and 0.017, and finally, it increases to 3.3 K at 0.023 Zn concentration. These results suggest that the change in the electronic structure induced by Zn doping is more important than the chemical pressure effects with regard to tuning the magnetic order. A study on the electronic structure and pressure tuning of the newly synthesized heavy-fermion compound $\text{CeRh}(\text{In}_{1-x}\text{Zn}_x)_5$, which does not include a toxic element, is expected to further enhance our understanding of the competing ground states emerging in heavy-fermion systems.

DOI: [10.1103/PhysRevMaterials.4.084801](https://doi.org/10.1103/PhysRevMaterials.4.084801)

I. INTRODUCTION

The interplay of superconductivity, magnetism, and quantum criticality has been an important issue in condensed-matter physics because it could lead to various emergent quantum states near $T = 0$ K. For example, magnetic fluctuations are believed to play a crucial role in the formation of unconventional superconductivity that is often observed in the proximity of a quantum critical point at which the magnetic order is suppressed to zero temperature by nonthermal parameters such as pressure, chemical substitution, and magnetic field [1,2]. Emphasizing the importance of quantum criticality, non-Fermi liquid behavior is observed in the normal state of unconventional superconductors [3,4].

Heavy-fermion compounds provide an excellent platform to study the consequence of the aforementioned interplay as their various ground states can be easily tuned via competition between the Ruderman-Kittel-Kasuya-Yosida (RKKY) and Kondo interactions [5]. In fact, continuous tuning between the different ground states has been observed via a series of studies on various substitutions for the In sites in the CeTIn_5 family ($T = \text{Co}, \text{Rh}, \text{and Ir}$). Sn substitution for In, as electron doping, monotonically suppresses the superconductivity (SC) and antiferromagnetism (AFM) in CeCoIn_5 [6,7] and CeRhIn_5 [8], respectively. The expected competing phases (AFM and SC) are not induced by the Sn doping. However, continuous tuning between the two competing states is achieved in hole-doped $\text{CeCo}(\text{In}_{1-x}\text{M}_x)_5$ ($M = \text{Zn}, \text{Cd}, \text{and}$

Hg) [9–12]. Being analogous with the results observed in systematic studies of isoelectronic substitution of Co or Ir for Rh sites [13–15], AFM in hole-doped compounds initially appears near the critical concentration where SC is completely suppressed. By increasing the doping concentration, two magnetic phases that correspond to incommensurate and commensurate magnetic structures have been suggested in $\text{CeRh}(\text{In}_{1-x}\text{Hg}_x)_5$ [10,16] and $\text{CeRh}(\text{In}_{1-x}\text{Cd}_x)_5$ [9,10]. Nuclear magnetic resonance (NMR) measurements [17], nuclear quadrupole resonance measurements [18], and soft x-ray-absorption spectroscopy measurements [19] suggest that the different local electronic environments around the doped atoms, i.e., the effects of inhomogeneous (Cd doping) versus homogeneous (Sn doping) on the electronic structure, could explain the different responses to electron and hole doping in these isostructural compounds. However, the origin of doping effects on ground states is still being debated [10,19]. To further explore the doping effects and elucidate the interplay between magnetism and superconductivity, in this study we synthesized single crystals of hole-doped $\text{CeRh}(\text{In}_{1-x}\text{Zn}_x)_5$, and characterized their physical properties via electrical resistivity, specific heat, and magnetic susceptibility for different field orientations, especially in comparison with those of electron-doped $\text{CeRh}(\text{In}_{1-x}\text{Sn}_x)_5$

II. EXPERIMENT METHODS

Single crystals of $\text{CeRh}(\text{In}_{1-x}\text{Zn}_x)_5$ were synthesized by the standard In flux method [7,8,10–12,16]. The high-quality starting materials, i.e., Ce (rod, 99.9%), Rh (powder, 99.99%), In (ingot, 99.999%), and Zn (shot, 99.99%), in the molar ratio

*tp8701@skku.edu

1 : 1 : $F(1-x)$: $F(x)$, with $F = 20$, were sealed in a quartz tube under vacuum. The tube was heated from room temperature to 1100 °C at a rate of 180 °C/h and maintained at this temperature for 12 h to obtain a homogeneous mixture. The tube was then cooled slowly at ~ 5 °C/h to 600 °C. Most of the excess In flux was removed by spinning the (inverted) tube in a centrifuge at 600 °C and ~ 2300 rpm. For $\text{CeRh}(\text{In}_{1-x}\text{Sn}_x)_5$, the same method was used with molar ratio 1 : 1 : 20 : y [8]. Single crystals with three-dimensional tetragonal blocks and well-defined facets (typical dimension $6 \times 6 \times 2$ mm³) were obtained for both $\text{CeRh}(\text{In}_{1-x}\text{Zn}_x)_5$ and $\text{CeRh}(\text{In}_{1-x}\text{Sn}_x)_5$ compounds.

Powder x-ray-diffraction patterns, which were analyzed using MDI JADE, showed that the tetragonal crystal structure is independent of Zn/Sn-doping levels. Energy-dispersive x-ray-spectroscopy measurements on single crystals determined that all the elements are distributed homogeneously and that the actual Zn and Sn concentration is approximately 16% of the nominal concentration and $x = 0.08y$, respectively, which are analogous with previous reports on $\text{CeRh}(\text{In}_{1-x}\text{Hg}_x)_5$ [10] and $\text{CeRh}(\text{In}_{1-x}\text{Sn}_x)_5$ [8]. Hereafter, the actual concentrations will be used throughout this paper. $\text{CeRh}(\text{In}_{1-x}\text{Zn}_x)_5$ crystals, with $x = 0, 0.001, 0.003, 0.008, 0.012, 0.017, \text{ and } 0.023$, and $\text{CeRh}(\text{In}_{1-x}\text{Sn}_x)_5$ crystals, with $x = 0, 0.024, 0.044, 0.060, 0.069, \text{ and } 0.084$, were synthesized successfully. Being similar to $\text{CeCo}(\text{In}_{1-x}\text{Zn}_x)_5$ [12], the absence of a stable CeRhZn_5 phase prevents the formation of higher-doped $\text{CeRh}(\text{In}_{1-x}\text{Zn}_x)_5$ ($x > 0.023$).

The newly synthesized Zn-doped compound $\text{CeRh}(\text{In}_{1-x}\text{Zn}_x)_5$ was investigated by measuring its electrical resistivity, specific heat, and magnetic susceptibility. For comparison, magnetic susceptibility measurements were also performed for $\text{CeRh}(\text{In}_{1-x}\text{Sn}_x)_5$. The standard four-probe method was used in the electrical resistivity measurements performed using the Physical Property Measurement System (Quantum Design), in the temperature range of 1.8 to 300 K, and using the ³He cryostat (Heliox VL, Oxford Instruments) at temperatures as low as 0.3 K. The specific heat was measured using a homemade calorimetry by employing a thermal relaxation method. A commercial superconducting quantum interference device magnetometer (MPMS, Quantum Design) with an external magnetic field of up to 5 T was used for the dc magnetization measurements in the temperature range of 1.8 to 356 K.

III. RESULTS AND DISCUSSION

A. X-ray-diffraction patterns

The results of the x-ray-diffraction measurements on $\text{CeRh}(\text{In}_{1-x}\text{Zn}_x)_5$ are displayed in Fig. 1, together with those of $\text{CeRh}(\text{In}_{1-x}\text{Sn}_x)_5$ for comparison. Except for the three peaks marked by red stars corresponding to the In flux, all other Bragg peaks in the substituted (Zn and Sn) samples can be indexed well based on the HoCoGa_5 -type tetragonal structure. The fitted lattice parameters a and c , and the unit-cell volume V as a function of concentration are shown in Figs. 1(b), 1(c), and 1(d), respectively. These results show that the lattice parameters a and c , and the unit-cell volume decrease continuously by 0.009 Å, 0.013 Å, and 0.54%, respectively, as

the Zn concentration increases from 0 to 0.023. In contrast, the lattice parameters and unit-cell volume of the Sn-doped $\text{CeRh}(\text{In}_{1-x}\text{Sn}_x)_5$ gradually increase with an increasing Sn concentration. The opposite responses observed for the Zn and Sn substitutions can be ascribed to their relative ionic radii.

B. Electrical resistivity and specific heat

The magnetic resistivity (ρ_{mag}) for $\text{CeRh}(\text{In}_{1-x}\text{Zn}_x)_5$, which was obtained by subtracting the nonmagnetic analog LaRhIn_5 , is shown in Fig. 2(a). As the Zn concentration increases, ρ_{mag} is enhanced over the whole measured temperature range owing to enhanced impurity scatterings caused by the Zn substitution. The temperature dependence of ρ_{mag} for all concentrations of Zn in $\text{CeRh}(\text{In}_{1-x}\text{Zn}_x)_5$ shows the typical trend of Ce-based Kondo lattice systems. With a decreasing temperature, ρ_{mag} follows logarithmic dependence, as shown by the fitting of $\rho_{\text{mag}} = \alpha - \beta \ln T$ [red lines in Fig. 2(a)]; this dependence arises from the incoherent Kondo scattering between conduction electrons and the $4f$ spins of the Ce^{3+} state [20]. It is notable that the slope (β) of $-\ln T$ remains almost constant within the experimental errors with respect to various Zn concentrations, as shown in the inset of Fig. 2(a), indicating that Kondo coupling does not change significantly under Zn doping [20]. This is in sharp contrast to the dependence on pressure, where the coupling strength is enhanced notably by applied pressure [21,22]. In the Doniach model, which captures the competition between RKKY and Kondo interactions [23], the ground state of heavy-fermion systems is determined by the product $JN(0)$, where J is the Kondo coupling coefficient that represents the hybridization strength between conduction electrons and localized spins (f electrons) and $N(0)$ is the electronic density of states at the Fermi level. The application of pressure tunes the ground state as a global parameter by changing the exchange coupling coefficient J . Being similar to other Cd and Hg hole dopings, on the other hand, Zn doping is expected to affect the local electronic environments to tune the ground state. The local doping effect is also supported by the high-pressure studies on $\text{CeRh}(\text{In}_{1-x}\text{Hg}_x)_5$ ($x = 0.0045$) [24], where the pressure-induced SC dome in Hg-doped CeRhIn_5 is not shifted from that of the undoped compound except for the suppression of superconducting transition temperatures owing to the breaking of Cooper pairs via disorder scattering.

With a further decrease in temperature, the logarithmically increasing resistivity reaches its maximum at T_{max} , marked by arrows in Fig. 2(a). Below T_{max} , the local incoherent scattering at each Kondo center (Ce^{3+} ions in this case) becomes coherent due to the periodic array of Kondo centers, and ρ_{mag} rapidly decreases with temperature. With increasing Zn concentration, T_{max} gradually decreases from ~ 53 K for pure CeRhIn_5 to ~ 25 K at 0.023 Zn. Another anomaly related to the AFM transition is observed at lower temperatures. The temperature dependence of ρ_{mag} is amplified near T_{N} in Fig. 2(b). The AFM transition temperature of 3.8 K in CeRhIn_5 initially decreases to 3.1 K for Zn-doping values up to 0.012. It is then nearly constant between Zn concentrations of 0.012 and 0.017, finally increasing to 3.3 K at 0.023 Zn,

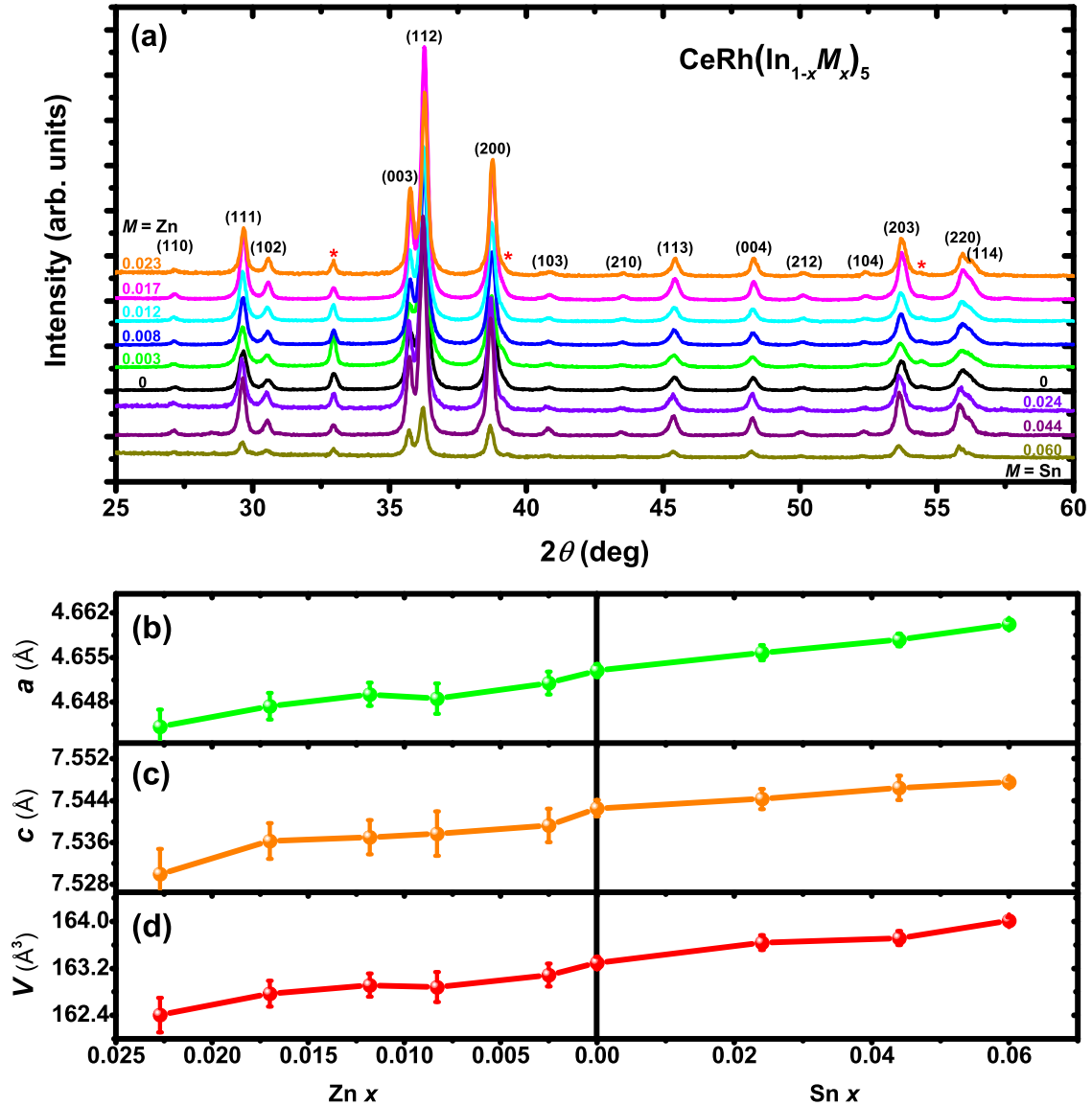


FIG. 1. (a) Powder x-ray-diffraction patterns for $\text{CeRh}(\text{In}_{1-x}\text{Zn}_x)_5$ ($0 \leq x \leq 0.023$) and $\text{CeRh}(\text{In}_{1-x}\text{Sn}_x)_5$ ($0 \leq x \leq 0.060$) collected at various doping concentrations. Red stars represent the indium flux. (b)–(d) Doping concentration dependences of the lattice parameters a , c and the unit-cell volume (V), respectively.

as shown in Fig. 2(d). The Zn concentration dependence of T_N was also confirmed by specific-heat measurements. The low-temperature $\text{Ce } 4f$ -electron contribution to specific heat divided by the temperature, C_{4f}/T , is plotted as a function of temperature for several representative Zn concentrations in Fig. 2(c), which is obtained after subtracting that of non-magnetic analog LaRhIn_5 [25]. The phase transition from the paramagnetic state to the AFM state is denoted by the lambda-like anomaly that is shifted to lower temperatures as the Zn concentration increases, and the anomaly remains sharp up to a Zn concentration of 0.017 and then it starts to broaden at 0.023 Zn. T_N as a function of Zn concentration determined by specific-heat measurements, as shown in Fig. 2(d), is consistent with the results obtained from resistivity measurements. The $4f$ contribution to the entropy S_{4f} is calculated by integrating C_{4f}/T over T . The temperature dependence of entropy S_{4f} is shown in the inset of Fig. 2(c). The magnetic entropy of

Zn-doped CeRhIn_5 series recovers to similar values above 5 K, suggesting that the strength of the hybridization does not change over the whole doping range studied in this work. The recovered entropy below T_N , however, increases with increasing Zn concentration, indicating that the extra magnetic entropy comes from the increased concentration of the unscreened Ce moments.

C. Magnetic susceptibility

The evolution of T_N with Zn doping (x) may be indicative of a change in the magnetic structure at a critical concentration between 0.012 and 0.017, where T_N becomes almost constant with respect to Zn doping [26]. The kinklike feature in the T - x phase diagram, as shown in Fig. 2(d), was also reported for other hole-doped compounds, i.e., $\text{CeRh}(\text{In}_{1-x}M_x)_5$ ($M = \text{Cd}, \text{Hg}$) [9,10,16]. The magnetic susceptibilities (χ)

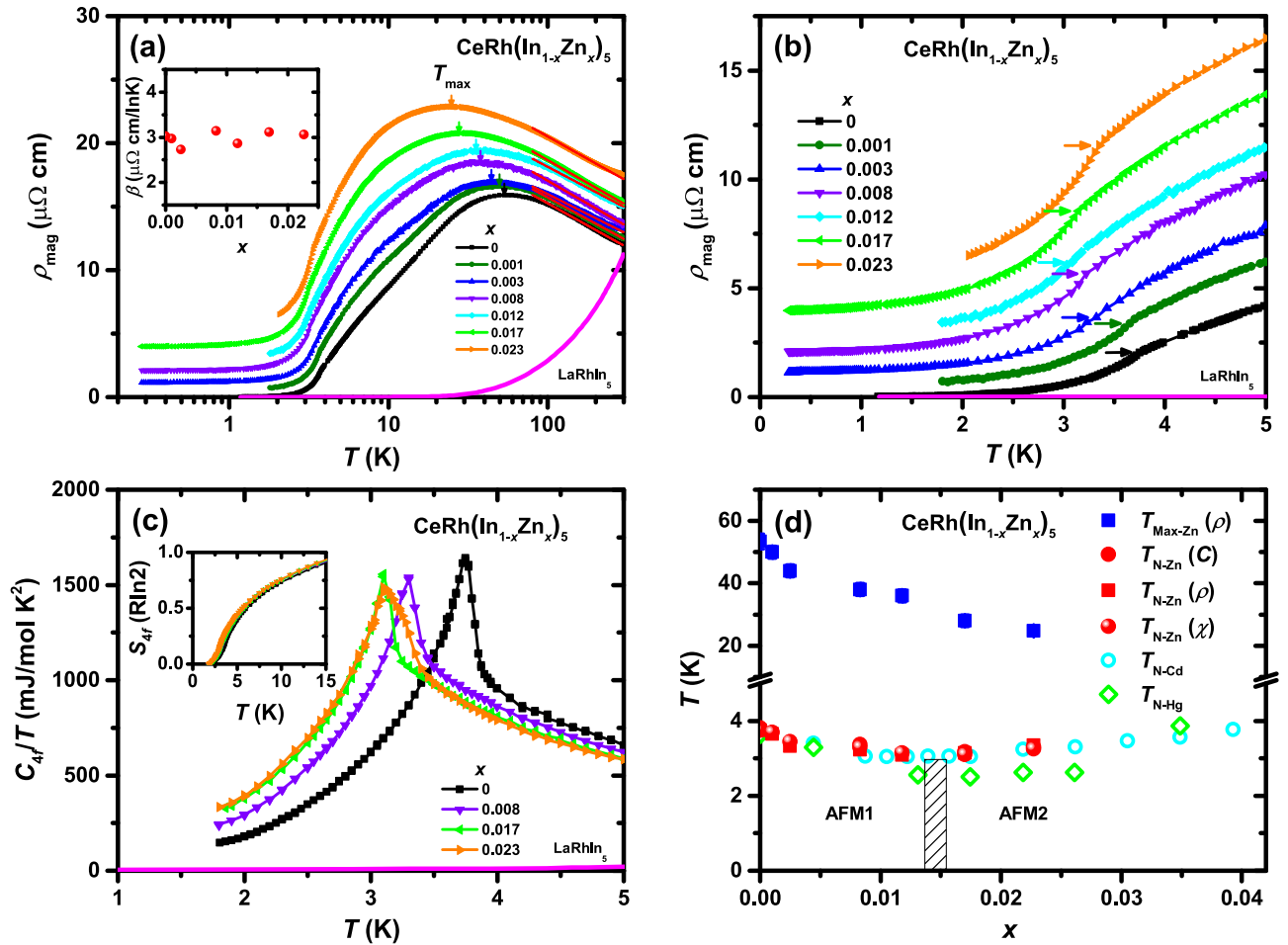


FIG. 2. (a) Temperature dependence of the magnetic contribution to electrical resistivity (ρ_{mag}) of $\text{CeRh}(\text{In}_{1-x}\text{Zn}_x)_5$ ($0 \leq x \leq 0.023$) for the current applied within the Ce-In plane. The values are plotted on a semilogarithmic scale. Electrical resistivity of the nonmagnetic analog LaRhIn_5 is also plotted for comparison. The peak temperature of ρ_{mag} (T_{max}) is marked by the arrows. The red solid lines are the least-squares fits of $\rho_{\text{mag}} = \alpha - \beta \ln T$ in the high- T regime. The inset shows the Zn concentration dependence of the slope β . (b) ρ_{mag} near the AFM transition region magnified on a linear scale, where the arrows indicate the AFM transition temperature (T_N). (c) $4f$ contribution to specific heat divided by temperature (C_{4f}/T) plotted as a function of temperature in the vicinity of T_N for representative Zn-doping levels in $\text{CeRh}(\text{In}_{1-x}\text{Zn}_x)_5$. The specific heat, C/T , of LaRhIn_5 is shown as a function of temperature, which is adopted from Ref. [25]. Inset shows the temperature dependence of recovered entropy due to $4f$ electrons. (d) T_N of $\text{CeRh}(\text{In}_{1-x}\text{M}_x)_5$ ($M = \text{Zn}, \text{Cd}, \text{and Hg}$) and the resistivity maximum temperature T_{max} of $\text{CeRh}(\text{In}_{1-x}\text{Zn}_x)_5$ plotted as a function of doping concentration x . For $\text{CeRh}(\text{In}_{1-x}\text{Zn}_x)_5$, the T_N values were obtained from resistivity measurements (red squares), specific-heat measurements (red circles), and susceptibility measurements (red balls). The data for $\text{CeRh}(\text{In}_{1-x}\text{Cd}_x)_5$ and $\text{CeRh}(\text{In}_{1-x}\text{Hg}_x)_5$ adopted from Ref. [10] are displayed by cyan circles and green diamonds, respectively. AFM1 and AFM2 represent two possible antiferromagnetic phases that have different magnetic structures.

of $\text{CeRh}(\text{In}_{1-x}\text{Zn}_x)_5$ with $0 \leq x \leq 0.023$ and $\text{CeRh}(\text{In}_{1-x}\text{Sn}_x)_5$ with $0 \leq x \leq 0.084$ are presented as functions of temperature on a semilogarithmic scale in Figs. 3(a) and 3(b), respectively, for a magnetic field ($H = 1$ kOe) applied parallel and perpendicular to the crystallographic c axis. In the high- T regime, where Kondo impurities provide dominant scatterings in the transport properties, both χ_{ab} and χ_c increase with decreasing temperature owing to Ce $4f$ -spin paramagnetism. The temperature dependence of the inverse magnetic susceptibility (χ^{-1}) is displayed in the insets of Figs. 3(a) and 3(b). The linear temperature dependence of χ^{-1} (the purple solid linear-fitting lines) indicates that neither Zn nor Sn doping affect the Curie-Weiss behavior in this Kondo impurity regime. The polycrystalline average susceptibility was estimated by $\chi_{\text{poly}} = (2/3)\chi_{ab} + (1/3)\chi_c$ for a tetrago-

nal structure, as shown in Figs. 3(c) and 3(d). From fits to the Curie-Weiss (CW) law $\chi = C/(T - \theta_{\text{CW}})$, the effective magnetic moment and the paramagnetic Curie-Weiss temperatures θ_{CW} (θ_{ab} , θ_c , and θ_{poly}) are summarized in Table I and Table II. The insets of Figs. 3(c) and 3(d) show the doping concentration dependence of θ_{CW} . The crystal-field effect may be responsible for the anisotropy of θ_{CW} (θ_{ab} and θ_c) in both Zn- and Sn-doping cases that is independent of the doping concentrations. With increasing Sn concentrations, θ_{ab} , θ_c , and θ_{poly} continuously decrease, while θ_{ab} , θ_c , and θ_{poly} almost do not change with Zn concentrations. The doping dependence of θ_{poly} indicates that within a molecular-field model Kondo coupling coefficient maintains nearly constant along the Zn-doping series, while it increases with increasing Sn concentrations [25]. With a further decrease in temperature, the

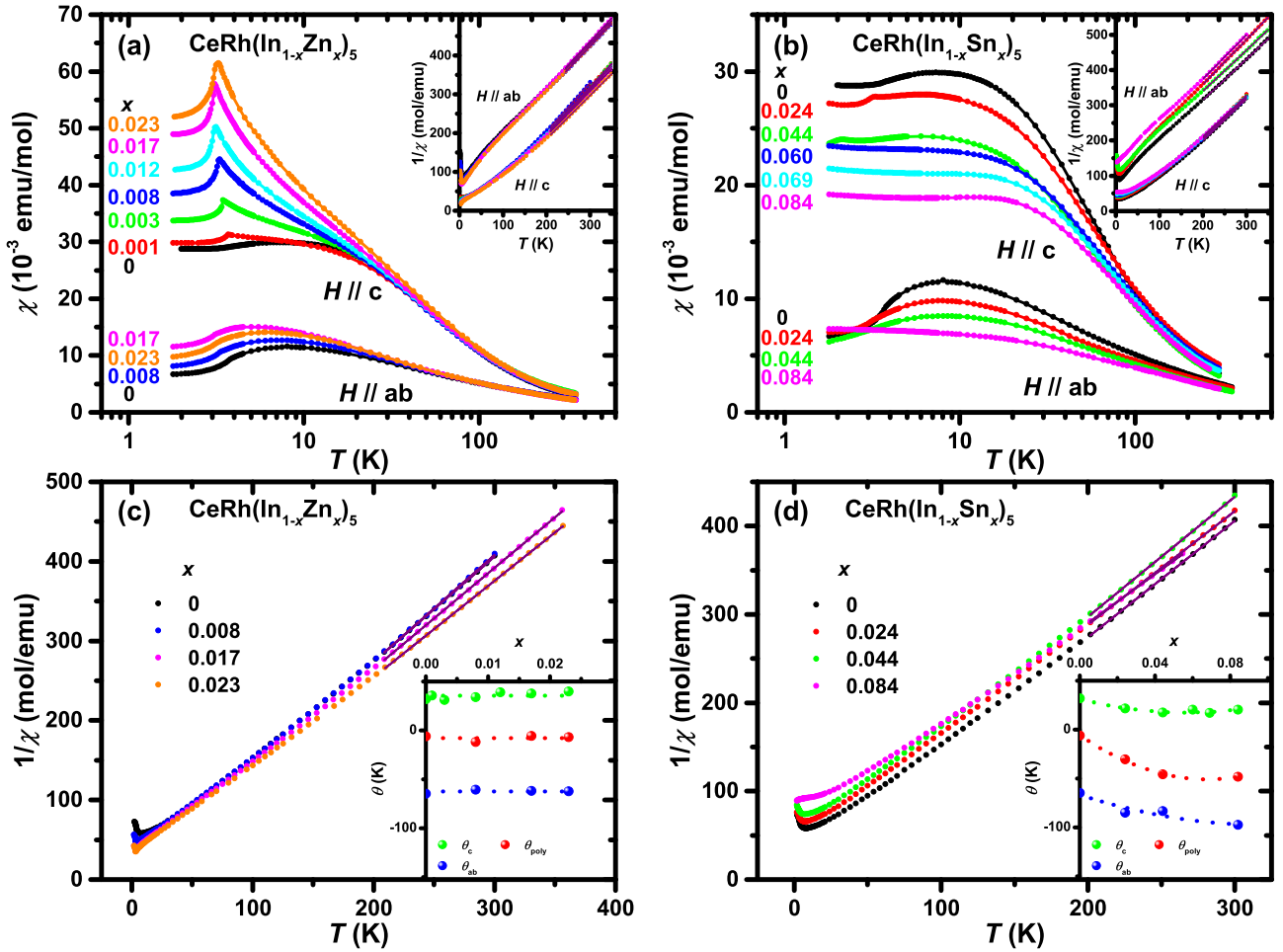


FIG. 3. Susceptibilities of $\text{CeRh}(\text{In}_{1-x}\text{M}_x)_5$ ($M = \text{Zn}, \text{Sn}$) plotted as a function of temperature on a semilogarithmic scale in (a) and (b), respectively. A magnetic field of 1 kOe was applied along the c axis and ab plane for both the Zn- and Sn-doped compounds. Insets show the temperature dependence of the inverse magnetic susceptibility (χ^{-1}). The inverse of polycrystalline average susceptibilities plotted as a function of temperature in (c) and (d) for $\text{CeRh}(\text{In}_{1-x}\text{M}_x)_5$ ($M = \text{Zn}, \text{Sn}$), respectively. Insets show the doping dependence of the Curie-Weiss temperatures θ_{CW} (θ_{ab} , θ_c , and θ_{poly}) obtained by fitting to Curie-Weiss law $\chi = C/(T - \theta_{CW})$. Purple solid lines are the linear fits of data at high-temperature regime. Dashed lines are guides to the eyes.

susceptibility is almost saturated near the Kondo coherence temperature, where the electrical resistivity shows a broad maximum.

For fields applied parallel and perpendicular to the Ce-In plane, χ increases with an increasing Zn-doping level, whereas it decreases with increasing Sn doping. This contrasting behavior could be ascribed to different changes in the

electronic structures induced by the substitution of Zn and Sn for In. Because Zn has one less electron than In, Zn doping locally reduces the hybridization strength near the Zn dopants, whereas Sn doping enhances hybridization because Sn has one more electron than In. In conformance with this scenario, the kinklike anomaly at 3.8 K, which arises due to the AFM transition in the pure compound, remains for Sn-doping cases

TABLE I. Effective magnetic moment (μ_{eff}) and Curie-Weiss temperature (θ_{CW}) of $\text{CeRh}(\text{In}_{1-x}\text{Zn}_x)_5$ compounds obtained from a Curie-Weiss fit to the high-temperature inverse susceptibility data as indicated by the purple lines in Fig. 3. Dashes represent samples that were not measured.

Zn	0	0.001	0.003	0.008	0.012	0.017	0.023
$\mu_{\text{eff}} (H c \text{ axis}) (\mu_B)$	2.601	2.579	2.621	2.547	2.587	2.612	2.648
$\mu_{\text{eff}} (H \perp c \text{ axis}) (\mu_B)$	2.605	—	—	2.611	—	2.577	2.613
$\mu_{\text{eff-poly}} (\mu_B)$	2.456	—	—	2.482	—	2.500	2.557
$\theta_{CW} (H c \text{ axis}) (\text{K})$	31.717	35.390	30.990	33.907	39.029	37.785	39.601
$\theta_{CW} (H \perp c \text{ axis}) (\text{K})$	-64.907	—	—	-60.587	—	-62.103	-62.269
$\theta_{CW\text{-poly}} (\text{K})$	-6.072	—	—	-11.849	—	-5.958	-6.934

TABLE II. Effective magnetic moment (μ_{eff}) and Curie-Weiss temperature (θ_{CW}) of $\text{CeRh}(\text{In}_{1-x}\text{Sn}_x)_5$ compounds obtained from a Curie-Weiss fit to the high-temperature inverse susceptibility data as indicated by the purple lines in Fig. 3. Dashes represent samples that were not measured.

Sn	0	0.024	0.044	0.060	0.069	0.084
$\mu_{\text{eff}} (H\parallel c \text{ axis}) (\mu_B)$	2.601	2.618	2.644	2.644	2.640	2.612
$\mu_{\text{eff}} (H\perp c \text{ axis}) (\mu_B)$	2.605	2.518	2.595	–	–	2.523
$\mu_{\text{eff-poly}} (\mu_B)$	2.456	2.551	2.653	–	–	2.651
$\theta_{\text{CW}} (H\parallel c \text{ axis}) (\text{K})$	31.717	21.326	17.303	20.112	16.897	20.272
$\theta_{\text{CW}} (H\perp c \text{ axis}) (\text{K})$	–64.907	–85.068	–83.517	–	–	–97.715
$\theta_{\text{CW-poly}} (\text{K})$	–6.072	–30.753	–45.796	–	–	–48.407

except that T_N is suppressed for both field orientations. For Zn-doped compounds, however, the kink feature in χ_c turns into a lambda-like sharp peak for $H\parallel c$, indicating that some fraction of Ce moments in the vicinity of Zn dopants was not well screened by conduction electrons, and thus, they act as impurity moments. The tendency of χ shows a contrasting behavior between the two field orientations at the critical Zn-doping concentration of 0.023: χ for $H\parallel c$ continuously increases with increasing Zn doping, whereas it starts to decrease for $H\parallel ab$. In addition, T_N is not constant anymore; instead, it starts to increase at the critical concentration. The change in the tendency of χ and the broadened heat capacity at 0.023 Zn may reflect a change in the magnetic structure of $\text{CeRh}(\text{In}_{1-x}\text{Zn}_x)_5$. To determine the magnetic structure, it is necessary to perform additional works such as neutron scattering or NMR measurements.

Figures 4(a) and 4(b) show the magnetic anisotropy of Zn- and Sn-doped compounds, respectively, between the two different field orientations, χ_c/χ_{ab} . Without regard to the type of dopants or doping levels, the anisotropy gradually increases with decreasing temperature in the high- T Kondo regime, which is similar to the results for nondoped CeRhIn_5 . Below T_{max} , where resistivity shows a maximum temperature, as shown in the insets to Fig. 4, the anisotropy is almost saturated to approximately 2.7 for both doped compounds, indicating that the crystalline c axis is the easy magnetic axis. With a further decrease in temperature, the anisotropy starts to increase again for both Sn- and Zn-doped compounds. For a 0.084 Sn, where T_N is completely suppressed, the anisotropy ratio is slightly decreased, indicating that the low- T additional anisotropy at lower doping concentrations arises from the tendency of the $4f$ spins of the Ce^{3+} ions to be ordered.

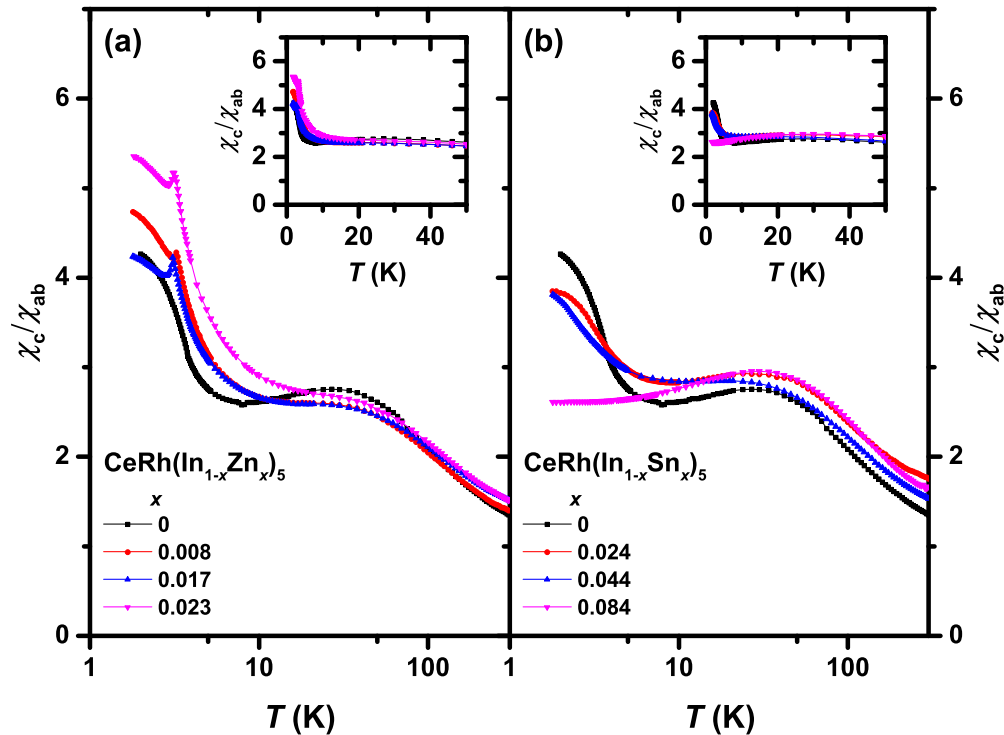


FIG. 4. Anisotropy of susceptibility for fields applied parallel and perpendicular to the crystalline c axis, χ_c/χ_{ab} , plotted as a function of temperature on a semilogarithmic scale in (a) and (b) for $\text{CeRh}(\text{In}_{1-x}M_x)_5$ ($M = \text{Zn}, \text{Sn}$), respectively. Insets are the low- T susceptibility ratios on a linear scale for temperatures below 50 K.

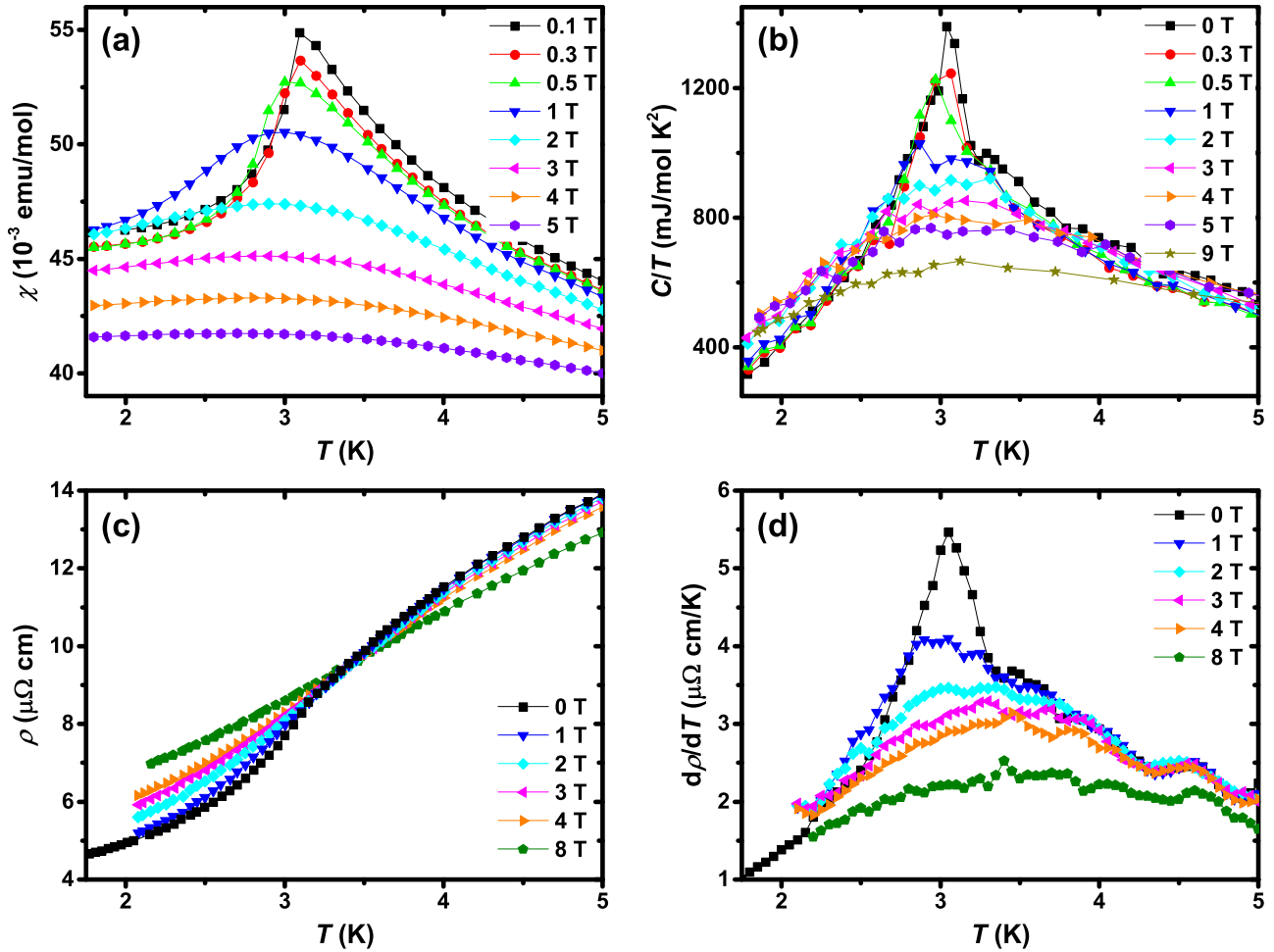


FIG. 5. Field dependence of antiferromagnetism for $\text{CeRh}(\text{In}_{0.983}\text{Zn}_{0.017})_5$ with magnetic field applied along the crystallographic c axis. Susceptibility, specific heat divided by temperature (C/T), resistivity, and the first temperature derivative of resistivity, $d\rho/dT$, for $\text{CeRh}(\text{In}_{0.983}\text{Zn}_{0.017})_5$ are plotted as a function of temperature under various magnetic fields in (a), (b), (c), and (d), respectively.

D. Antiferromagnetic order under a magnetic field

Magnetic-field dependence of the antiferromagnetic state of $\text{CeRh}(\text{In}_{0.983}\text{Zn}_{0.017})_5$ has been probed by the magnetic susceptibility, specific heat, and electrical resistivity under various magnetic fields applied along the crystallographic c axis. As shown in Fig. 5(a), the low-temperature susceptibility reveals a pronounced lambda-like peak at 3.1 K, corresponding to the AFM transition at $B = 0.1$ T. With the increase of magnetic field, this peak shifts to lower temperature, while maintaining its sharpness up to 0.5 T. For magnetic fields higher than 1 T, however, the peak anomaly switches to a broad maximum and the phase transition is not obvious anymore. Figure 5(b) displays the specific heat divided by temperature (C/T) as a function of temperature, where a peak anomaly is observed at T_N and C/T at 5 K is close to 600 mJ/mol K^2 , indicating that the 1.7% Zn-doped compound is a heavy-fermion compound. Being similar to the magnetic susceptibility, the peak remains sharp up to 0.5 T, but becomes broadened at higher fields, suggesting that there is no obvious long-range AFM phase above 0.5 T. Electrical resistivity is

additionally measured to elucidate the evolution of T_N under magnetic field and plotted as a function of temperature in Fig. 5(c). The first derivative of the resistivity with respect to the temperature is shown in Fig. 5(d), where a clear transition point is observed at 0 T. The broad peak that occurs at higher fields increases with increasing field. Taken together, these transport as well as thermodynamic measurements underscore that the paramagnetic to AFM phase transition takes place up to 0.5 T, but there may occur a field-induced spin-polarized state at higher magnetic fields [27,28]. In addition, the similar field dependence was also observed for $x = 0.023$ case (not shown), which raises a possibility that 0.023 doping case may share the same magnetic structure with that of 0.017 doping case.

E. Discussion

The doping dependence of T_N for $\text{CeRh}(\text{In}_{1-x}\text{M}_x)_5$ ($M = \text{Zn}, \text{Cd}, \text{and Hg}$) is summarized in Fig. 2(d). The T_N response to Zn substitution is similar to that of other hole-doped cases ($M = \text{Cd}, \text{Hg}$). Chemical substitution can induce chemical

pressure as well as changes in the electronic structure. The unit-cell volume of $\text{CeRh}(\text{In}_{1-x}\text{Zn}_x)_5$ decreases with an increasing Zn concentration, implying that Zn acts as a positive chemical pressure. The effective pressure, $\Delta P = 0.32$ GPa, can be estimated if we assume that lattice parameters shift rigidly from CeRhIn_5 to $\text{CeRh}(\text{In}_{0.983}\text{Zn}_{0.017})_5$ by using the bulk modulus of CeRhIn_5 [29]. Even though the estimated ΔP is expected to increase T_N by ~ 0.1 K with Zn doping [30], T_N decreases by 0.7 K, suggesting that the electronic structure tuning induced by substitution is more relevant in determining T_N than the chemical pressure. The lack of change in the Kondo coupling strength with increased Zn doping is consistent with the importance of the electronic structure in determining T_N . We propose that the effect of Zn substitution on the magnetic order could be understood by its local doping effects, where local magnetic droplets are nucleated surrounding the Zn dopants, while the remaining region outside the droplets is unaffected [17–19]. For low Zn concentrations ($x \leq 0.008$), the short correlation length between magnetic droplets may not be sufficient enough to induce an additional long-range magnetic order. However, the local magnetic droplets could compete with the existing antiferromagnetic phase (AFM1), leading to the decrease of AFM1 order. With increasing the Zn concentration, the distance between the droplets becomes shorter and eventually compatible with the correlation length, thus forming a long-range order (AFM2). Finally, AFM2 is enhanced with further increasing Zn doping ($x \geq 0.017$). The slight differences among different hole dopants may arise from the different sizes of local magnetic droplets. Additional microscopic measurements such as NMR will be important to prove the presence of magnetic droplets in the Zn-doped CeRhIn_5 , as was reported in the Cd-doped CeCoIn_5 [17–19].

IV. SUMMARY

In summary, we successfully synthesized Zn-doped $\text{CeRh}(\text{In}_{1-x}\text{Zn}_x)_5$ in the doping range from $x = 0$ to 0.023. The x-ray powder-diffraction study showed that the lattice parameters and unit-cell volume decrease with an increasing Zn-doping concentration, indicating the positive pressure effect. Electrical resistivity, specific heat, and magnetic susceptibility measurements showed that the antiferromagnetic ordering temperature is initially suppressed, becoming nearly constant between Zn concentrations of 0.012 and 0.017. With a further increase in Zn doping, T_N increases at Zn concentrations higher than $x = 0.017$. The magnetic susceptibility of Zn-doped CeRhIn_5 is enhanced with an increase in the doping concentration, and the kinklike feature at T_N turns into a sharp lambda-like peak. However, the magnetic susceptibility (χ) of the Sn-doped compounds is suppressed with an increase in the doping concentration. When combined with the anticorrelation between T_N and the unit-cell volume, the contrasting results observed for the Sn and Zn dopants suggest that changes in the electronic structure surrounding the local dopants are more important than the chemical pressure effects in controlling the competing ground states. The synthesized heavy-fermion compound $\text{CeRh}(\text{In}_{1-x}\text{Zn}_x)_5$ will stimulate more studies on the electronic structure and pressure-tuning effects to explore the mechanism of the competing ground states emerging in heavy-fermion systems.

ACKNOWLEDGMENTS

This work was supported by the National Research Foundation (NRF) of Korea by a grant funded by the Korean Ministry of Science and ICT (Grant No. 2012R1A3A2048816).

-
- [1] E. Dagotto, *Rev. Mod. Phys.* **66**, 763 (1994).
 [2] J. Paglione and R. L. Greene, *Nat. Phys.* **6**, 645 (2010).
 [3] H. v. Löhneysen, A. Rosch, M. Vojta, and P. Wölfle, *Rev. Mod. Phys.* **79**, 1015 (2007).
 [4] G. R. Stewart, *Rev. Mod. Phys.* **73**, 797 (2001).
 [5] C. Pfleiderer, *Rev. Mod. Phys.* **81**, 1551 (2009).
 [6] E. D. Bauer, C. Capan, F. Ronning, R. Movshovich, J. D. Thompson, and J. L. Sarrao, *Phys. Rev. Lett.* **94**, 047001 (2005).
 [7] E. D. Bauer, N. O. Moreno, D. J. Mixson, J. L. Sarrao, J. D. Thompson, M. F. Hundley, R. Movshovich, and P. G. Pagliuso, *Physica B* **359–361**, 35 (2005).
 [8] E. D. Bauer *et al.*, *Physica B* **378–380**, 142 (2006).
 [9] L. D. Pham, T. Park, S. Maquilon, J. D. Thompson, and Z. Fisk, *Phys. Rev. Lett.* **97**, 056404 (2006).
 [10] C. H. Booth *et al.*, *Phys. Rev. B* **79**, 144519 (2009).
 [11] M. Yokoyama *et al.*, *Phys. Rev. B* **92**, 184509 (2015).
 [12] M. Yokoyama, K. Fujimura, S. Ishikawa, M. Kimura, T. Hasegawa, I. Kawasaki, K. Tenya, Y. Kono, and T. Sakakibara, *J. Phys. Soc. Jpn.* **83**, 033706 (2014).
 [13] P. G. Pagliuso, C. Petrovic, R. Movshovich, D. Hall, M. F. Hundley, J. L. Sarrao, J. D. Thompson, and Z. Fisk, *Phys. Rev. B* **64**, 100503(R) (2001).
 [14] J. R. Jeffries, N. A. Frederick, E. D. Bauer, H. Kimura, V. S. Zapf, K. D. Hof, T. A. Sayles, and M. B. Maple, *Phys. Rev. B* **72**, 024551 (2005).
 [15] A. Llobet *et al.*, *Phys. Rev. Lett.* **95**, 217002 (2005).
 [16] E. D. Bauer, F. Ronning, S. Maquilon, L. D. Pham, J. D. Thompson, and Z. Fisk, *Physica B* **403**, 1135 (2008).
 [17] R. R. Urbano, B. L. Young, N. J. Curro, J. D. Thompson, L. D. Pham, and Z. Fisk, *Phys. Rev. Lett.* **99**, 146402 (2007).
 [18] H. Sakai, F. Ronning, J. X. Zhu, N. Wakeham, H. Yasuoka, Y. Tokunaga, S. Kambe, E. D. Bauer, and J. D. Thompson, *Phys. Rev. B* **92**, 121105(R) (2015).
 [19] K. Chen, F. Strigari, M. Sundermann, Z. Hu, Z. Fisk, E. D. Bauer, P. F. S. Rosa, J. L. Sarrao, J. D. Thompson, J. Herrero-Martin *et al.* *Phys. Rev. B* **97**, 045134 (2018).
 [20] B. Cornut and B. Coqblin, *Phys. Rev. B* **5**, 4541 (1972).
 [21] Z. Ren, G. W. Scheerer, D. Aoki, K. Miyake, S. Watanabe, and D. Jaccard, *Phys. Rev. B* **96**, 184524 (2017).
 [22] Z. Ren, L. V. Pourovskii, G. Girit, G. Lapertot, A. Georges, and D. Jaccard, *Phys. Rev. X* **4**, 031055 (2014).

- [23] S. Doniach, *Physica B+C* **91**, 231 (1977).
- [24] S. Seo, S. Ju, T. Park, E. D. Bauer, and J. D. Thompson, *Prog. Supercond.* **14**, 17 (2012).
- [25] P. F. S. Rosa, A. Oostra, J. D. Thompson, P. G. Pagliuso, and Z. Fisk, *Phys. Rev. B* **94**, 045101 (2016).
- [26] G. Knebel, D. Aoki, G. Lapertot, B. Salce, J. Flouquet, T. Kawai, H. Muranaka, R. Settai, and Y. Ōnuki, *J. Phys. Soc. Jpn.* **78**, 074714 (2009).
- [27] A. Steppke *et al.*, *Science* **339**, 933 (2013).
- [28] Y. Luo, F. Ronning, N. Wakeham, X. Lu, T. Park, Z. A. Xu, and J. D. Thompson, *Proc. Natl. Acad. Sci. USA* **112**, 13520 (2015).
- [29] R. S. Kumar, A. L. Cornelius, and J. L. Sarrao, *Phys. Rev. B* **70**, 214526 (2004).
- [30] T. Park, E. D. Bauer, and J. D. Thompson, *Phys. Rev. Lett.* **101**, 177002 (2008).